Research Square

Preprints are preliminary reports that have not undergone peer review.
They should not be considered conclusive, used to inform clinical practice,
or referenced by the media as validated information.

# Macrophage membrane camouflaged puerarin and probucol co-assembled nanoparticles for targeted anti-atherosclerosis therapy

**Yan Gao**
Chongqing Medical University
**Yangyang Bai**
Chongqing Medical University
**Jieying Zeng**
Chongqing Medical University
**Yinuo Wang**
Chongqing Medical University
**Yuxin Zhang**
Chongqing Medical University
**Mengjie Jia**
The First Affiliated Hospital of Chongqing Medical University
**Yajie Guo**
Chongqing Medical University
**Juhui Qiu**
Chongqing University
**Yiliang Li**
The Eighth Affiliated Hospital of Sun Yat-Sen University
**Li Fu**
The Eighth Affiliated Hospital of Sun Yat-Sen University
**Guixue Wang**
Chongqing University
**Yi Wang**
wangyi@cqmu.edu.cn

Chongqing Medical University https://orcid.org/0009-0001-8989-9280

**Research Article**

**Keywords:** Atherosclerosis, Biomimetic nanoparticles, Traditional Chinese medicine component, Targeted drug delivery, Combined therapy

**Posted Date:** September 28th, 2026

**DOI:** https://doi.org/10.21203/rs.3.rs-10939219/v1

**License:** This work is licensed under a Creative Commons Attribution 4.0 International License.
Read Full License

# Macrophage membrane camouflaged puerarin and probucol co-assembled nanoparticles for targeted anti-atherosclerosis therapy

Yan Gao[a,1], Yangyang Bai[a,1], Jieying Zeng[a,1], Yinuo Wang[b], Yuxin Zhang[a], Mengjie Jia[c], Yajie Guo[a], Juhui Qiu[e], Yiliang Li[f], Li Fu[g,*], Guixue Wang[d,e,*], Yi Wang[a,d,*]

[a] *School of Basic Medical Sciences, Chongqing Medical University, Chongqing, 400016, China.*

[b] *Chongqing Medical University-University of Leicester Joint Institute, Chongqing Medical University, Chongqing, 400016, China.*

[c] *Department of Critical Care Medicine, The First Affiliated Hospital of Chongqing Medical University, Chongqing 400010, China.*

[d] *JinFeng Laboratory, Chongqing, 401329, China.*

[e] *Key Laboratory for Biorheological Science and Technology of the Ministry of Education, National Local Joint Engineering Lab for Vascular Implants, College of Bioengineering, Chongqing University, Chongqing, 400044, China.*

[f] *The Eighth Affiliated Hospital of Sun Yat-sen University, Shenzhen 518033, China.*

[g] *Geriatrics Department, Neurological Rehabilitation Department, The Eighth Affiliated Hospital of Sun Yat-sen University, Shenzhen 518033, China.*

[1] Co-first authors: Yan Gao, Yangyang Bai and Jieying Zeng

*Co-Corresponding author: Li Fu − The Eighth Affiliated Hospital of Sun Yat-sen University, Shenzhen 518033, China; Geriatrics Department, Neurological Rehabilitation Department, The Eighth Affiliated Hospital of Sun Yat-sen University, Shenzhen 518033, China; Email: fuliruo302@163.com

*Co-Corresponding author: Guixue Wang − JinFeng Laboratory, Chongqing, 401329, China; Key Laboratory for Biorheological Science and Technology of the Ministry of Education, National Local Joint Engineering Lab for Vascular Implants, College of Bioengineering, Chongqing University, Chongqing, 400044, China; Email: wanggx@cqu.edu.cn

*Corresponding author: **Yi Wang** − School of Basic Medical Sciences, Chongqing Medical University, Chongqing, 400016, China; JinFeng Laboratory, Chongqing, 401329, China; Email: wangyi@cqmu.edu.cn

## Abstract

**Background:**Atherosclerosis (AS), characterized by chronic arterial inflammation and plaque formation, is a leading global cause of morbidity and mortality due to its progression to coronary artery disease and stroke. Oxidative stress, apoptosis, and lipid deposition at AS lesion sites are recognized key drivers of disease progression. In this study, we developed a biomimetic nanotherapeutic platform integrating a traditional Chinese medicine (TCM) component co-assembly strategy with cell membrane encapsulation technology for targeted AS therapy.

**Methods:**Specifically, puerarin (PR) and probucol (PB) were co-assembled into nanoparticles (PR@PBNPs) using a simple nanoprecipitation method. To enhance targeting specificity to atherosclerotic plaques, macrophage membrane-camouflaged PR@PBNPs (MPR@PBNPs) were further engineered.

**Results:**Comprehensive in vitro evaluations demonstrated that MPR@PBNPs effectively ameliorated oxidative stress, apoptosis, and lipid uptake in both endothelial cells and macrophages. In AS mouse models, MPR@PBNPs preferentially accumulated in atherosclerotic plaques, substantially inhibiting lesion progression of AS.

**Conclusion:**This biomimetic nanoplatform combines the advantages of TCM component self-assembly with cell membrane-mediated targeting, establishing a promising therapeutic strategy for AS.

**Keywords：** Atherosclerosis; Biomimetic nanoparticles; Traditional Chinese medicine component; Targeted drug delivery; Combined therapy

## 1. Introduction

AS, a chronic inflammatory disease characterized by lipid accumulation and plaque formation within arterial walls, predominantly affects critical vasculature such as the

coronary, carotid, and cerebral arteries. This condition leads to high-risk cardiovascular disorders, including coronary heart disease and stroke, posing a significant threat to human health [1-3]. Current clinical management of AS primarily includes pharmacological therapy, interventional procedures (e.g., stent placement), and surgical interventions [4, 5]. However, these conventional treatments exhibit limitations. Pharmacological therapy often suffers from low drug utilization efficiency and adverse effects due to long-term administration; vascular stent interventions carry risks of restenosis and late in-stent thrombosis; and surgical interventions are invasive, potentially traumatic, and may involve complications [6, 7]. Therefore, developing novel therapeutic approaches for AS holds substantial value and research significance.

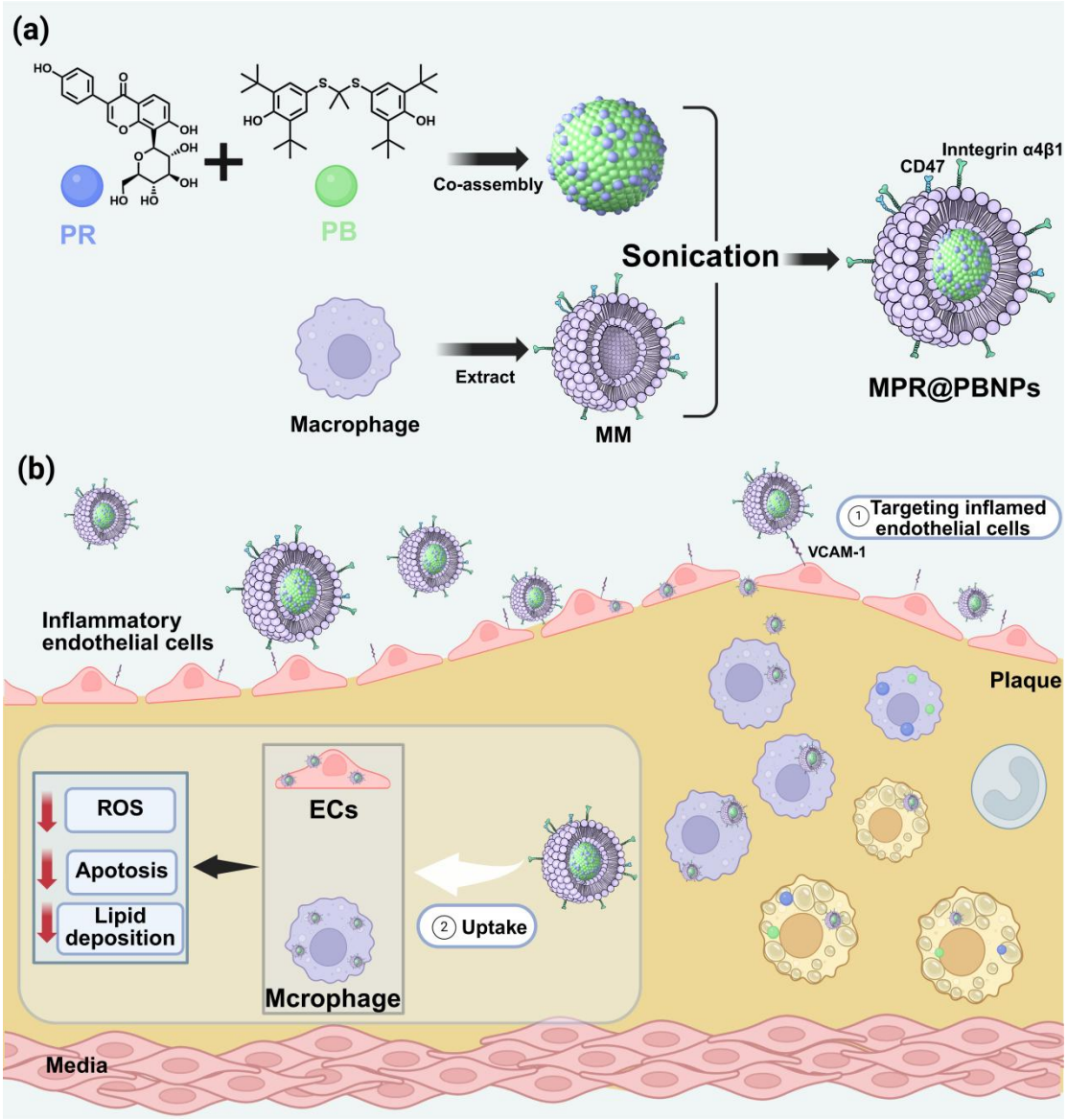
Nanomedicines leverage nanoscale engineering to modulate drug physicochemical properties, pharmacodynamics, and pharmacokinetic profiles, demonstrating superior therapeutic efficacy and reduced off-target effects compared to conventional formulations [8-10]. These advantages position nanomedicines as promising candidates for combating AS [11]. Despite significant advances, current developed AS-targeted nanotherapeutics face limitations, including complex preparation routes, dependency on exogenous carriers that constrain drug-loading capacity, and inadequate lesion-specific targeting resulting in suboptimal biodistribution [12-14]. TCM component self-assembled nanoparticles (NPs) represent an innovative drug delivery technology, formed through the intrinsic self-assembly properties of active TCM-derived components [15, 16]. A key advantage is their high drug-loading efficiency, enabling effective therapeutic agent delivery. Moreover, by eliminating the need for nanocarriers, this approach avoids potential carrier-associated adverse reactions and simplifies preparation [17]. Therefore, this study leverages TCM component self-assembly technology to develop a new targeted nanoplatform for AS therapy.

Extensive research demonstrates that oxidative stress, apoptosis, and lipid deposition play pivotal roles in AS progression. Consequently, antioxidant therapy combined with inhibition of apoptosis and lipid deposition represents an ideal strategic approach for AS management [18-20]. PR, a major bioactive isoflavone extracted from Pueraria lobata root, exhibits antioxidant, anti-apoptotic, and anti-inflammatory properties,

conferring protective effects against vascular dysfunction [21, 22]. Clinically, PR is widely utilized in China and other Asian countries for treating cardiovascular diseases. Furthermore, PR's intrinsic amphiphilic nature enables self-assembly into micelles in aqueous environments, facilitating hydrophobic therapeutic encapsulation [23]. PB, an FDA-approved hydrophobic antioxidant, demonstrates potent anti-atherosclerotic efficacy [24, 25]. Capitalizing on these complementary properties, we engineered PR and PB co-assembled NPs via TCM component self-assembly, achieving high co-loading efficiency.

Cell membrane camouflage technology endows NPs with inherent biological functionality by transferring source cell-specific membrane proteins to synthetic cores [26-28]. This biomimetic approach exploits native ligand-receptor recognition systems embedded in membrane proteins, enabling active homing to pathological microenvironments [29, 30]. Critically, macrophages serve as central orchestrators in AS pathogenesis and express characteristic surface proteins enabling specific recognition of AS lesion sites [31, 32]. Therefore, coating NPs with macrophage membranes (MM) enhances targeting efficacy to atherosclerotic lesions.

Herein, we integrate TCM component self-assembly with cell membrane-coating technology to construct a novel biomimetic nanotherapeutic platform for efficient and safe AS therapy (Scheme 1). Specifically, PR and PB were co-assembled into PR@PBNPs via nano-precipitation. Subsequently, extracted MM were coated onto PR@PBNPs via sonication to prepare the biomimetic nanoformulation (MPR@PBNPs). The MM coating enables MPR@PBNPs to efficiently target and accumulate within AS lesions. Within plaques, MPR@PBNPs were internalized by endothelial cells and macrophages to ameliorating oxidative stress, apoptosis, and lipid deposition, thereby achieving potent anti-atherosclerotic efficacy with enhanced safety.




**Scheme 1.** (a) PR and PB were co-assembled into PR@PBNPs by the nano-precipitation method. MPR@PBNPs were further prepared by coating MM onto PR@PBNPs by sonication. (b) MPR@PBNPs effectively targeted and accumulated at atherosclerotic lesion sites, and were internalized by endothelial cells and macrophages to alleviate oxidative stress, apoptosis, and lipid accumulation, thereby enabling effective AS therapy.

## 2. Materials and methods

### 2.1. Materials

PR was purchased from Shanghai Aladdin Biochemical Technology Co., L TD. (Shanghai, China). PB was purchased from Shanghai Maclean Biochemical Co., LTD. (Shanghai, China). 1,1' -octadecanediphenyl-3,3,3',3' -tetramethyl-dicar bonyl-4-chlorobenzesulfonate (DiD) was purchased from Beijing Best Biotechnol ogy Co., LTD. (Beijing, China). The CCK-8 detection kit (Cell Counting Kit-8) was purchased from APExBIO Technology LLC (Shanghai, China). Anti-CD68 polyclonal antibody and anti-integrin β1 polyclonal antibody were purchased fr om Wuhan Protein Technology Biotechnology Co., LTD. (Wuhan, China). Rabb it anti-integrin α4 and rabbit anti-CD47 antibodies were purchased from Cell Si gnaling Technology in the United States (USA). Hoechst 33342, Reactive Oxyg en Species (ROS) detection kit, calcein-AM/PI Double staining Kit, and LysoTr acker Green DND-26 were purchased from Dalian Meilun Biotechnology Co., LTD. (Dalian, China). The Oil Red O (ORO) staining kit was purchased from Solarbio Technology Co., LTD. (Beijing, China). TNF-α was purchased from B eijing Zhongnuo Biotechnology Co., LTD. (Beijing, China). Lipopolysaccharide (LPS) and tert-butyl peroxide (TBHP) were purchased from Sigma-Aldrich (US A). Oxidized low-density lipoprotein (ox-LDL) was purchased from Guangzhou Yuanyi Biotechnology Co., LTD. (Guangzhou, China).

### 2.2. Optimization of PR@PBNPs preparation

PB and PR were dissolved in 1 mL of N,N-dimethylformamide (DMF) at differ ent quality ratios (1:1, 2:1, 1:2). Each organic solution was then individually added dropwise into 4 mL of pure water under stirring at 500 rpm. The resulting mixtures were transferred into dialysis bags (MWCO: 3500) and dialyzed against pure water overnight to remove unassembled PB and PR as well as organic solvent. After dialy sis, the aqueous dispersions of PR@PBNPs prepared at different quality ratios were collected. The hydrodynamic diameter and polydispersity index (PDI) of the prepared PR@PBNPs were measured using dynamic light scattering (DLS) (90Plus PALS, B rookhaven, USA).

### 2.3. Preparation of PR@PBNPs

PR@PBNPs were prepared by the nano-precipitation method. Accurately weigh 5 mg of PR, 10 mg of PB, and 1mg of DSPE-$PEG_{2k}$-COOH and dissolve them in 1 mL of DMF solution. The above organic solvent was added dropwise into 4 mL of stirred pure water (500 rpm). Then, the mixture was transferred to a dialysis bag (MWCO:3500), and dialysed in pure water overnight. The prepared PR@PBNPs solution was stored at 4 °C. To prepare DiD-labeled NPs, 3 μL of 1 mg/mL DiD solution was added to the organic phase, and DiD-labeled PR@PBNPs (DiD-PR@PBNPs) were prepared in the same manner as described above.

2.4. Fourier transform infrared (FTIR) spectroscopy

A certain amount of PR, PB, and a physical mixture of PR and PB powders, along with PR@PBNPs powder, were individually weighed, homogeneously mixed with dried KBr, and ground into fine powders before being pressed into pellets. The pellets were then scanned 32 times using an FTIR spectrometer (iS10, Nicolet, USA) under the following conditions: a wavenumber range of 500-4000 $cm^{-1}$, a resolution of 4 $cm^{-1}$, and a signal-to-noise ratio of 50,000:1. All spectra were subsequently processed using Origin 2018 software.

2.5. Investigation of Urea, NaCl, and sodium lauryl sulfate (SDS) effects on PR@PBNPs assembly

During the preparation of PR@PBNPs, intermolecular interaction disruptors (Urea, NaCl, or SDS) were individually added to 4 mL of ultrapure water, each at a final concentration of 50 mM. The organic phase containing PR and PB in 1 mL of DMF was then dropwise introduced into the aforementioned aqueous solution. After dialysis, the hydrodynamic diameter and PDI of the resulting PR@PBNPs were determined by DLS.

2.6. Molecular dynamics (MD) simulations

All MD simulations were performed using the GROMACS software package with the GAFF force field. The system was first optimized through energy minimization, followed by sequential equilibration in the NVT and NPT ensembles with gradual heating to 298 K. Final equilibration was conducted at 298.15 K and 1 atm, employing the Parrinello–Rahman barostat and the velocity rescaling thermostat. Electrostatic interactions were treated using the Particle Mesh Ewald (PME) method, while van der Waals interactions were computed with a 1.2 nm cutoff and dispersion correction. Simulations utilized the leap-frog integration algorithm with a 1 fs time step for a total duration of 20 ns. Hydrogen bonds were constrained using the LINCS algorithm, and the neighbor list was updated every 10 steps. Trajectory visualization was implemented

using OVITO and VMD, while data analysis was performed with custom Python scripts.

2.7. Acquisition of MM

RAW264.7 cells were cultured in a cell culture flask until approximately 90% fused. Then, the cells were collected and centrifuged in centrifuge tubes (2000 rpm, 5 min) to obtain cell precipitates. The cell precipitates were resuspended in 1×PBS. Subsequently, the cell suspension was placed in liquid nitrogen for repeated freezing and thawing five times. After grounding 20 times using a glass homogenizer to fully break the cells, the cell suspension was centrifuged at 1000 rpm for 10 minutes. Then, the supernatant was collected and centrifuged at 14,000 rpm for 20 minutes to obtain the MM precipitate. The protein content of the obtained MM was measured using the BCA protein concentration determination kit.

2.8. Preparation of MPR@PBNPs

PR@PBNPs and MM solution were mixed in a quality ratio of 9:1. Then, the mixture was treated in an ultrasonic water bath for 3 min (UC-6, Titan, China). DiD-labeled MPR@PBNPs (DiD-MPR@PBNPs) were prepared using the same method as mentioned above.

2.9. Characterization of NPs

The hydrodynamic diameter, zeta-potential, and morphology of PR@PBNPs and MPR@PBNPs were detected by DLS, Zeta potential meter, and TEM (Tecnai G2 12, FEI, USA). Subsequently, the hydrodynamic diameter of PR@PBNPs and MPR@PBNPs over 4 days in pure water, PBS, and medium containing 10% FBS was tested to characterize their stability.

2.10. Cytotoxicity test

RAW264.7 cells or HUVECs were inoculated into 96-well plates at a density of $1 \times 10^4$ cells per well. After culturing for 12 h, the cells were incubated with different concentrations of PR@PBNPs and MPR@PBNPs (10, 50, 100, 150, and 200 μg/mL) for 24 h. After incubating with CCK-8 for 30 minutes, the absorbance of each well was measured at 450 nm using a microplate reader (51119180ET, Thermo Fisher, China). The cell vitality computation formula is as follows:

Cell vitality (%) = (treatment group OD - blank OD) / (blank control group OD - group OD) × 100%

2.11. Hemolysis test

1 mL of mice anticoagulant blood was mixed with 1.25 mL of 1×PBS to obtain diluted anticoagulant blood. 1 mL of 1 mg/mL PR@PBNPs or MPR@PBNPs solution was added to each tube. In the negative control group, 1 mL of 1×PBS was added to each tube. In the positive control group, 1 mL of pure water was added to each tube. Then, 20 μL of diluted anticoagulant was added to each sample. After incubation at 37°C for 1 hour, the samples were centrifuged at 2000 rpm for 5 minutes. The supernatant of each sample was collected and measured the absorbance at a wavelength of 545 nm using a microplate reader. The hemolysis rate was calculated according to the following formula.

Hemolysis rate (%) = (OD of experimental group - OD of negative control group) / (OD of positive control group - OD of negative control group) × 100%.

2.12. Characterization of protein on MPR@PBNPs

The protein composition was characterized via sodium dodecyl sulfate–polyacrylamide gel electrophoresis (SDS–PAGE). First, the RAW264.7 cells, MM, MPR@PBNPs, and PR@PBNPs were lysed with RIPA lysis buffer containing PMSF for 3 min, and placed on ice for 30 min. Then the lysates were centrifuged, and the loading buffer was added to the supernatant, then denatured at 100°C for 10 min. A 20 μL protein sample was loaded onto a 10% SDS–PAGE gel and run at 50 V for 45 min, then run at 110 V for 60 min. The Coomassie blue staining solution was used to stain the protein bands. The protein bands were visualized with a Gel DocTM EZ system (Bio-Rad, USA).

For western blot, the protein samples were electrophoresed on an 8% SDS–PAGE gel. A Bio-Rad electrophoresis system was used to separate the proteins. The proteins were then transferred to PVDF membranes and blocked in 5% nonfat milk solution for 2 h. Then incubate with primary antibodies (anti-CD47, anti-CD68, anti-integrin α4, and anti-integrin β1) at 4°C overnight. Finally, the samples were immersed in the corresponding secondary antibodies for 1.5 h at room temperature. Protein signals were determined by a chemiluminescence imaging system (ChemiScole 6200 Touch, Clinx, China).

2.13. Macrophage and endothelial cell uptake of NPs

RAW264.7 cells were inoculated at 3 × $10^5$ cells per well in confocal dishes and cultured for 12 h. The cells were treated with LPS (treatment concentration 1 μg/mL) for 24 h. Then DiD-PR@PBNPs and DiD-MPR@PBNPs (the dosage was 66.7 μg/mL for PB and 33.3 μg/mL for PR) were added to each well for 2 h. The cells' nuclei were stained using Hoechst. Finally, the cells were observed using a confocal microscope (SP8, Leica, Germany). For flow cytometry analysis, the RAW264.7 cell suspension was prepared after incubating with the DiD-PR@PBNPs and DiD-MPR@PBNPs. Then, the cell suspension was detected using flow cytometry (CytoFLEX, Beckman Coulter, USA).

HUVECs were inoculated at 3 × $10^5$ cells per well in confocal dishes and cultured for 12 h. The cells were treated with TNF-α (treatment concentration 10 ng/mL) for 12 h. Subsequently, the cells were incubated with DiD-PR@PBNPs and DiD-MPR@PBNPs (the dosage was 66.7 μg/mL for PB and 33.3 μg/mL for PR) for 30 min. After removing the medium, the cells' nuclei were stained using Hoechst. Finally, the cells were observed using confocal microscopy. For flow cytometry analysis, the HUVECs suspension was prepared after incubating with DiD-PR@PBNPs and DiD-MPR@PBNPs. Then, the HUVECs suspension was detected using flow cytometry.

2.14. In vitro transwell model

HUVECs were implanted in the upper chamber of the transwell chamber (14152, Corning, America), and RAW264.7 cells were implanted in the lower chamber. HUVECs and RAW264.7 cells were stimulated with TNF-α (treatment concentration of 10 ng/mL) for 12 h. Then, DiD-PR@PBNPs and DiD-MPR@PBNPs (the dosage was 66.7 μg/mL for PB and 33.3 μg/mL for PR) were added in the upper chamber for 24 h. The RAW264.7 cells were fixed at room temperature with 4% paraformaldehyde for 5 minutes. After the cell nuclei were stained using DAPI, the RAW264.7 cells were observed using a confocal microscope. For flow cytometry analysis, the RAW264.7 cell suspension from the lower chamber was prepared after incubating with NPs. Then, the RAW264.7 cell suspension was detected using flow cytometry.

2.15. Suppressing ROS production in vitro

RAW264.7 cells were inoculated into 24-well plates at a density of $4\times10^5$ cells per well. After culturing for 12 h, LPS (treatment concentration 1 μg/mL) was added to stimulate the cells for 24 h. Subsequently, the cells in each group were treated with the free PR-PB, PR@PBNPs, and MPR@PBNPs (the dosage was 33.3 μg/mL for PB and 16.7 μg/mL for PR) for 9 h, respectively. The intracellular ROS were stained using DCFH-DA, and the cell nuclei were stained using Hoechst. Finally, the cells were observed with a microscope (DM3000, Leica, Germany). For flow cytometry analysis, after the cells were stained with DCFH-DA, the cell suspension was prepared. Then, the ROS levels in the RAW264.7 cells were detected by flow cytometry.

HUVECs were inoculated into 24-well plates at a density of $4\times10^5$ cells per well. After culturing for 12 h, the cells were stimulated with LPS (1 μg/mL) for 4 hours. Then, the cells were treated with the free PR-PB, PR@PBNPs, and MPR@PBNPs (the dosage was 33.3 μg/mL for PB and 16.7 μg/mL for PR) for 6 h. The intracellular ROS were stained using DCFH-DA, and the cell nuclei were stained using Hoechst. Finally, the cells were photographed using a microscope. For flow cytometry analysis, after cells were stained with DCFH-DA, the cell suspensions were prepared, and the ROS levels in HUVECs were detected by flow cytometry.

2.16. MPR@PBNPs inhibit cell uptake of ox-LDL

RAW264.7 cells or HUVECs were inoculated in 96-well plates at a density of $5\times10^3$ cells per well, respectively. After culturing for 12 h, cells were pretreated with free PR-PB, PR@PBNPs, and MPR@PBNPs (the dosage was 33.3 μg/mL for PB and 16.7 μg/mL for PR) for 4 h. Subsequently, the cells were treated with ox-LDL (at a treatment concentration of 50 μg/mL) for 12 h. Finally, the cells were stained with ORO and observed with a microscope.

2.17. Anti-apoptotic ability of MPR@PBNPs in vitro

RAW264.7 cells or HUVECs were seeded in 24-well plates at a density of $4\times10^5$ cells per well. After culturing for 12 h, cells were pretreated with free PR-PB, PR@PBNPs, and MPR@PBNPs at treatment concentrations of 50 μg/mL for

4 h (the dosage was 33.3 μg/mL for PB and 16.7 μg/mL for PR). Subsequently, the cells were treated with TBHP (5 mM) for 2 h. Then the cells were stained using AM and PI. Subsequently, the cells were observed with a microscope. For flow cytometry analysis, after the cells were stained with AM and PI, the cell suspensions were prepared, and the apoptosis of the cells was detected by flow cytometry.

2.18. Lysosomal escape

RAW264.7 cells or HUVECs were inoculated into confocal culture dishes (14152, Corning, America) (density $3 \times 10^5$ cells per dish). After culturing for 12 h, DiD-PR@PBNPs and DiD-MPR@PBNPs (the dosage was 33.3 μg/mL for PB and 16.7 μg/mL for PR) were added to the dishes. After treatment for 2 h or 6 h, the lysosome and the cell nucleus were stained by LysoTracker and Hoechst, respectively. Finally, the cells were observed using a confocal microscope.

2.19. RNA sequencing

RAW264.7 cells were seeded in 6-well plates at a density of $3 \times 10^5$ cells per well and cultured for 24 hours. The cells were then subjected to treatment with TNF-α (10 ng/mL) and ox-LDL (50 μg/mL), concurrently with MPR@PBNPs (the dosage was 33.3 μg/mL for PB and 16.7 μg/mL for PR). After 12 hours of treatment, total RNA was extracted from the harvested cells. All RNA samples underwent high-throughput sequencing on the Illumina NovaSeq 6000 (NovaSeq X Plus) platform.

2.20. In vivo targeting ability

Male ApoE$^{-/-}$ mice were raised on a high-fat diet for 7 weeks to establish the AS mouse model. To verify the targeting effect of nanomedicines on AS lesion plaques, 200 μL DiD-PR@PBNPs and DiD-MPR@PBNPs solutions were injected into AS model mice via the tail vein (dose of PB 5 mg/kg, PR 2.5 mg/kg). Twenty-four hours later, the mice were sacrificed, and their aorta and major organs (heart, liver, spleen, lung, and kidney) were obtained. Then, the aorta and major organs were imaged using a small animal live imaging system (NightOWL II LB 983, Berthold, Germany) at an excitation wavelength of 640 nm.

2.21. The in vivo therapy effect of MPR@PBNPs

Male ApoE$^{-/-}$ mice were raised on a high-fat diet for 7 weeks to establish the AS model. The AS model mice were divided into 4 groups. Each group was treated by tail vein injection of PR+PB every 3 days (free group), PR@PBNPs and MPR@PBNPs for 45 days (injection dose of PB 5 mg/kg, PR 2.5 mg/kg), while maintaining a high-fat diet throughout the treatment. After the treatment was completed, the mice were anesthetized and sacrificed. The entire aorta was isolated and fixed with 4% paraformaldehyde. Then, the aorta was stained with ORO and imaged with a microscope. Additionally, the section of the aorta root was prepared. Subsequently, the sections were stained with ORO, TB, and Masson. Meanwhile, immunohistochemistry staining of α-SMA and CD68 was performed on the sections. Finally, the stained sections were photographed using a stereomicroscope.

2.22. In vivo animal experiments to investigate the safety evaluation of MPR@PBNPs in AS mice

After the treatment was completed, the blood of the mice was obtained. The blood routine levels of mice were tested, and the levels of total cholesterol (CHO), triglycerides (TG), glutathione aminotransferase (ALT), aspartate aminotransferase (AST), blood urea nitrogen (BUN), and creatinine (CREA) in the blood were also measured. Finally, the hearts, livers, spleens, lungs, and kidneys of the mice were obtained and fixed with 4% paraformaldehyde. After preparing their paraffin sections, hematoxylin-eosin (H&E) staining was performed. Finally, the H&E sections were photographed using a stereomicroscope.

2.23. Statistics

In this study, all data were presented as mean ± standard deviation (Means ± SD). When processing and analyzing the experimental data, two software programs, GraphPad Prism 8.0 and Origin 2018, were used. When multiple groups of experimental samples are compared with each other, One-way ANOVA, a statistical method, is adopted. For the comparison of the two groups of experimental samples, the Student's t-test was used. In terms of judging the significance of data differences, based on the P value, when the P value is less than 0.05, it is considered that there are significant differences among the groups of data. The specific degree of difference is

represented by *$P \leqslant 0.05$, **$P \leqslant 0.01$, and ***$P \leqslant 0.001$, respectively.

## 3. Results and discussion

### 3.1. Optimization of PR@PBNPs preparation and assembly mechanism

PR@PBNPs were prepared using the nanoprecipitation method at varying quality ratios of PB to PR (1:1, 1:2, and 2:1). DLS measurements revealed that the PR@PBNPs prepared at a PB-to-PR quality ratio of 2:1 exhibited the smallest hydrodynamic size (Fig. 1A-B). Therefore, this 2:1 quality ratio was selected for the preparation of PR@PBNPs in all subsequent experiments. FTIR spectroscopy confirmed the presence of characteristic absorption peaks for both PR and PB in the PR@PBNPs, indicating the successful incorporation of both components into the NPs (Fig. 1C). To investigate the self-assembly mechanism of PR@PBNPs, SDS, Urea, and NaCl were introduced during the preparation process to disrupt hydrophobic interactions, hydrogen bonding, and electrostatic interactions, respectively. DLS analysis showed that all three agents induced changes in the particle size and PDI of the resulting PR@PBNPs, suggesting that hydrophobic interactions, hydrogen bonds, and electrostatic forces are potentially involved in the assembly process (Fig. S1). Furthermore, MD simulations were employed to analyze the assembly mechanism between PR and PB. The results demonstrated that over a 20 ns simulation, PB and PR formed aggregates and eventually reached a stable assembled state (Fig. 1D-E). Concurrently, the potential energy of the system gradually decreased as the self-assembly proceeded (Fig. S2). Importantly, the MD simulations indicated that the assembly of PB and PR was primarily driven by hydrogen bonding and π–π stacking (Fig. 1F). These results collectively demonstrate that PB and PR can form nanoaggregates at a quality ratio of 2:1, and that their self-assembly is mainly driven by hydrogen bonding and π–π stacking.

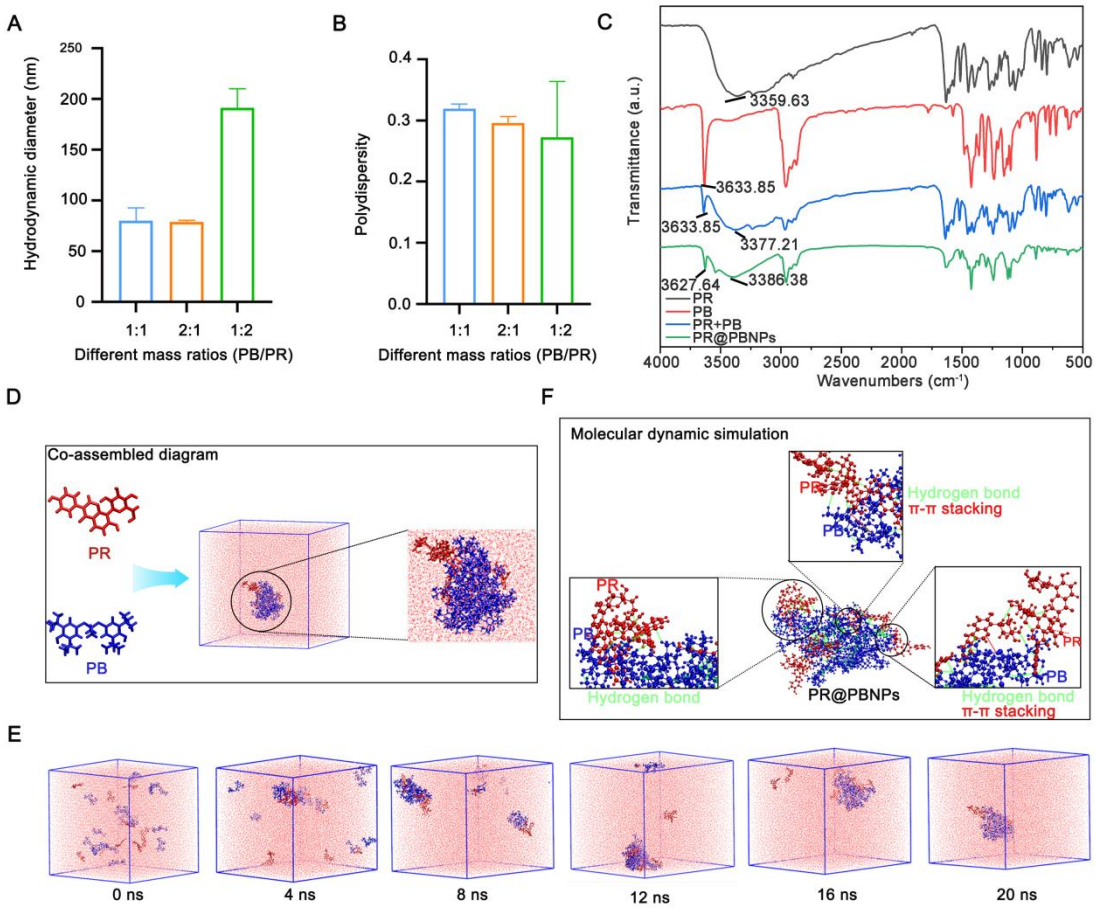



**Figure 1.** Optimization of Preparation and Assembly Mechanism of PR@PBNPs. (A) Particle size and (B) PDI of PR@PBNPs prepared at different quality ratios of PB to PR. (C) FTIR spectra of PB powder, PR powder, a physical mixture of PB and PR, and lyophilized PR@PBNPs powder. (D) Schematic illustration of the co-assembly between PB and PR. (E) Self-assembly process of PR@PBNPs in aqueous solution at different simulation times (0–20 ns). (F) Intermolecular interactions in the PR@PBNPs co-assembly process.

### 3.2. Preparation and characterization of MPR@PBNPs

PR@PBNPs were prepared via the nanoprecipitation method. DLS measurement revealed that the hydrodynamic diameter of PR@PBNPs was 98.51 ± 0.80 nm (Fig. 2A), with a PDI of 0.14 ± 0.01 (Fig. 2C) and a zeta potential of −24.28 ± 2.98 mV (Fig. 2B). Transmission electron microscopy (TEM) imaging confirmed that PR@PBNPs exhibited a uniform spherical morphology (Fig. 2D). Additionally, the isolated MM displayed a hydrodynamic diameter of 272.50 ± 6.15 nm (Fig. 2A), a PDI of 0.26 ±

0.003 (Fig. 2C), and a zeta potential of −38.45 ± 0.44 mV (Fig. 2B). TEM imaging shows that MM exhibits a distinct cell membrane structure (Fig. 2E). These results confirm the successful preparation of PR@PBNPs and extraction of MM. Subsequently, MM was coated onto PR@PBNPs via a sonication method to develop MPR@PBNPs. The resulting MPR@PBNPs exhibited a hydrodynamic diameter of 123.32 ± 3.64 nm (Fig. 2A) and a PDI of 0.19 ± 0.03 (Fig. 2C), indicating an increased hydrodynamic diameter of approximately 24.81 nm compared to the uncoated PR@PBNPs. The zeta potential of MPR@PBNPs was −38.22 ± 0.20 mV (Fig. 2B), closely matching that of the MM. TEM imaging further confirmed the presence of a distinct cell membrane bilayer coating on the surface of MPR@PBNPs (Fig. 2F), providing direct visual evidence of successful MM encapsulation. Furthermore, both PR@PBNPs and MPR@PBNPs exhibited negligible variations in hydrodynamic diameter and zeta potential when stored in water, 1× PBS, and 10% serum-containing media over 4 days, demonstrating their good stability (Fig. S3). These findings conclusively demonstrate the successful fabrication of MPR@PBNPs with uniform nanoscale dimensions and good stability.

The retention of proteins on MPR@PBNPs is critical for their biofunctional performance. SDS-PAGE was employed to analyze the protein profiles of macrophages, isolated MM, MPR@PBNPs, and PR@PBNPs. As shown in Fig. 2G, MPR@PBNPs have a similar protein composition to MM. In addition, we performed Western blot analysis to detect the characteristic proteins on macrophages, MM, and MPR@PBNPs, and PR@PBNPs. The CD68 protein, a macrophage marker, was detected on macrophages, MM, and MPR@PBNPs. Notably, the CD47 protein, which interacts with the SIRP-α receptor to deliver a "don’t eat me" signal, and the integrin α4/β1, which specifically recognizes VCAM-1 overexpressed on inflamed endothelial cells, were identified on MPR@PBNPs (Fig. 2H). These findings demonstrate that MPR@PBNPs retain the proteins from MM, enabling MPR@PBNPs to execute the biofunction of targeting AS lesion sites.

To preliminarily assess the biosafety of PR@PBNPs and MPR@PBNPs, their cytotoxicity and hemocompatibility were evaluated. Both PR@PBNPs and

MPR@PBNPs showed no significant effects on the viability of macrophages or HUVECs at treatment concentrations below 200 μg/mL, while exhibiting moderate pro-proliferative activity (Fig. S4). This effect may originate from the cell proliferation-promoting bioactivity of PR [33]. In vitro hemolysis assay confirmed that neither PR@PBNPs nor MPR@PBNPs induced hemolysis even at a high concentration of 1 mg/mL (Fig. S5). These results demonstrate the favorable cytocompatibility and hemocompatibility of PR@PBNPs and MPR@PBNPs.

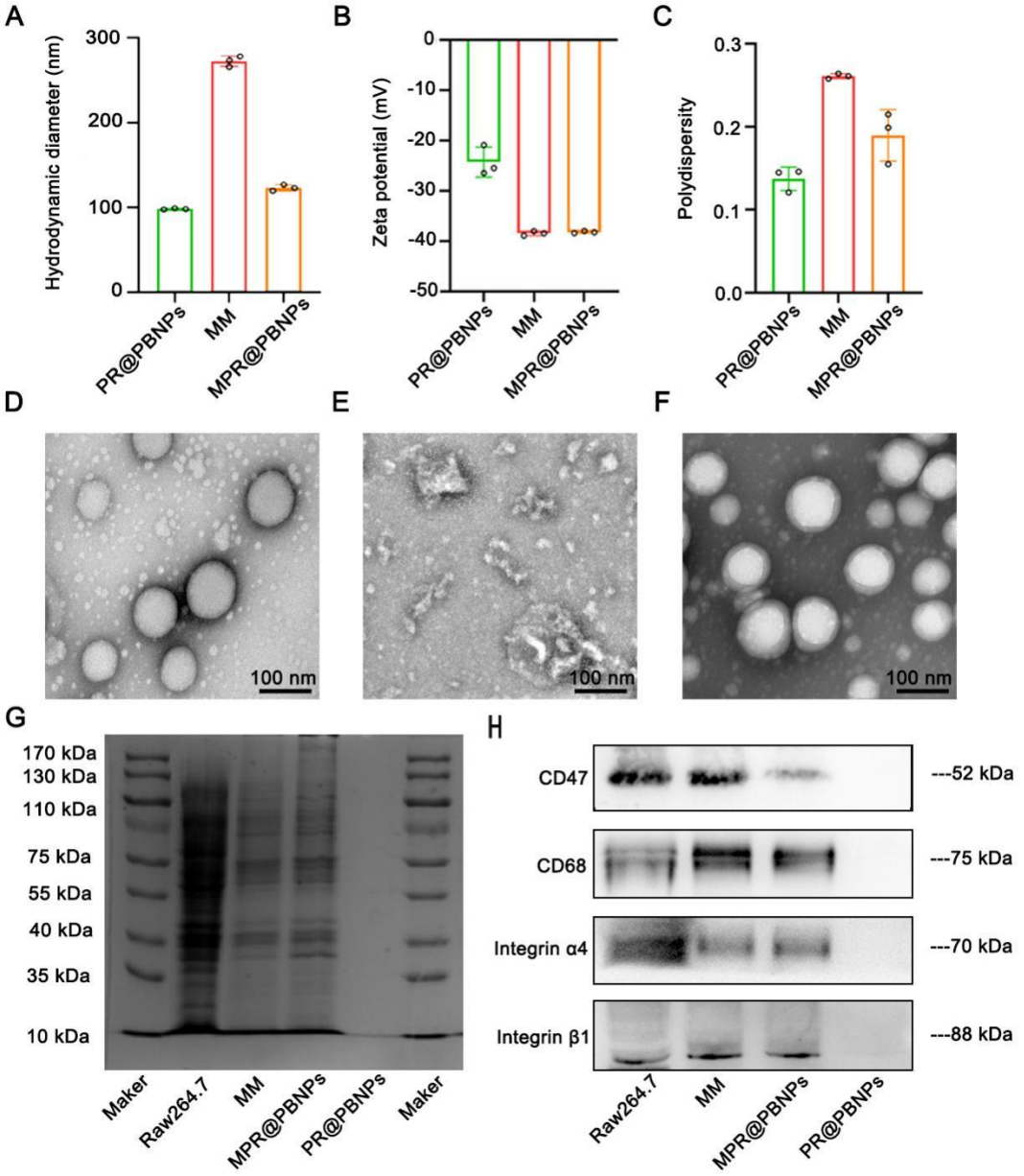



**Figure 2.** Characterization of the MPR@PBNPs. (A) The hydrodynamic diameters (B), zeta potentials, and (C) PDI of RR@PBNPs, MM, and MPR@PBNPs (*n*=3, mean ± SD). TEM images of PR@PBNPs (D), MM (E), and MPR@PBNPs (F) (scale bar: 100 nm). (G) Coomassie brilliant

blue analysis of protein component in RAW264.7, MM, MPR@PBNPs, and RR@PBNPs. (H) Western blot assay of CD47, CD68, integrin α4, and integrin β1 in RAW264.7, MM, MPR@PBNPs, and RR@PBNPs.

### 3.3. MPR@PBNPs enhance the uptake of endothelial cells and efficiently penetrate the endothelial layer

To effectively target atherosclerotic plaque regions, NPs must be efficiently internalized by endothelial cells and traverse the endothelial layer. In this study, the uptake of NPs by endothelial cells was first evaluated in vitro. HUVECs activated by TNF-α were co-incubated with DiD-labeled PR@PBNPs and MPR@PBNPs. The cellular uptake of these NPs was quantitatively assessed using confocal laser scanning microscopy (CLSM) and fluorescence-activated cell sorting (FACS). Compared to DiD-PR@PBNPs, DiD-MPR@PBNPs exhibited significantly stronger red fluorescence signals in TNF-α-activated HUVECs (Fig. 3A-C), indicating that MPR@PBNPs enhance their uptake by inflamed endothelial cells. Furthermore, an in vitro Transwell model was established to investigate the capacity of NPs to penetrate the endothelial layer. CLSM imaging revealed that RAW264.7 cells in the lower chamber internalized a greater amount of DiD-MPR@PBNPs compared to DiD-PR@PBNPs (Fig. 3D). FACS analysis confirmed a 1.2-fold higher uptake of DiD-MPR@PBNPs relative to DiD-PR@PBNPs by RAW264.7 cells (Fig. 3E-F). Collectively, these findings demonstrate that MPR@PBNPs are efficiently internalized by inflamed endothelial cells and can successfully traverse the endothelial layer.

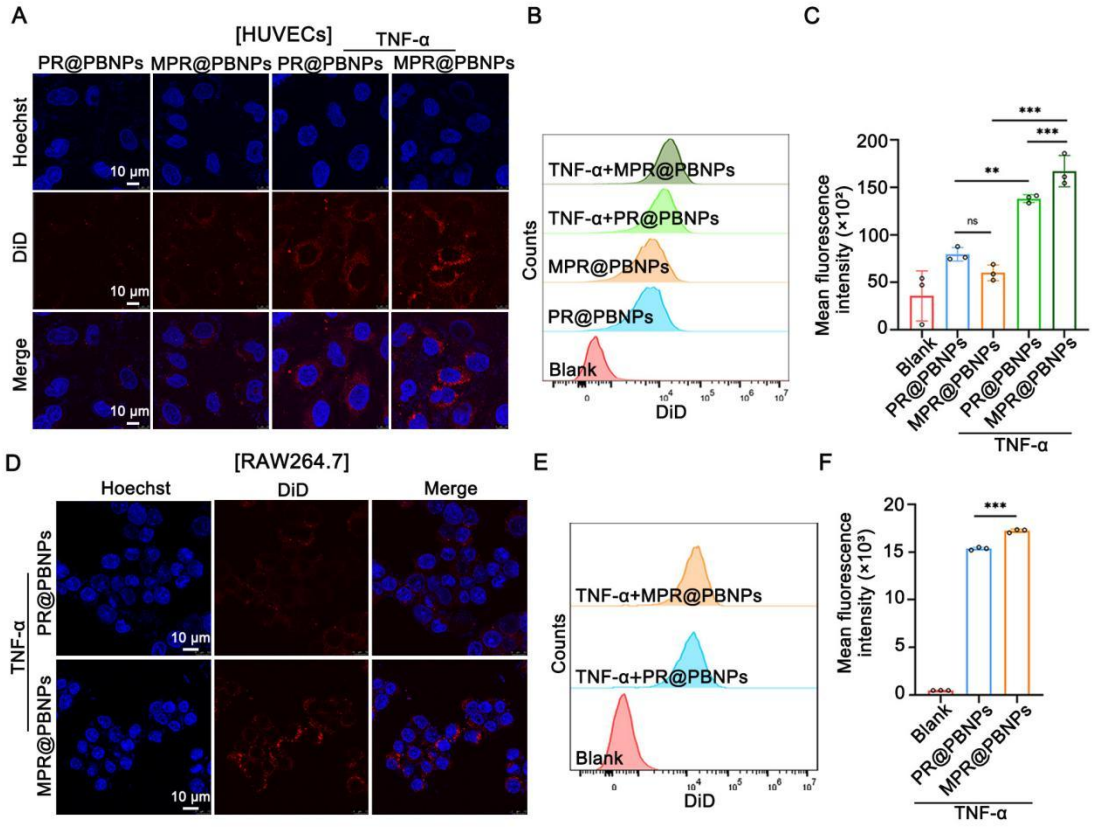



**Figure 3.** Endothelial cell uptake and trans-endothelial layer functionality. (A) CLSM images showing DiD-labelled PR@PBNPs and MPR@PBNPs internalization by TNF-α-activated or non-activated HUVECs (scale bar: 10 μm). (B) FACS analysis profiles and (C) quantitative mean fluorescence intensity of DiD-labelled PR@PBNPs and MPR@PBNPs internalization by TNF-α-activated or non-activated HUVECs ($n$=3, mean ± SD). (D) CLSM images of DiD-labelled PR@PBNPs and MPR@PBNPs internalized by activated RAW264.7 cells in the lower chamber (scale bar: 10 μm). (E) FACS analysis profiles and (F) quantitative mean fluorescence intensity of DiD-labelled PR@PBNPs and MPR@PBNPs internalized by activated RAW264.7 cells in the lower chamber ($n$=3, mean ± SD). Statistical significance: *$p$<0.05, **$p$<0.01, ***$p$<0.001; *ns*, no significance.

### 3.4. MPR@PBNPs inhibit ROS production, apoptosis, and lipid uptake in endothelial cells

Typically, nanomedicines need to enter the cytoplasm to exert their therapeutic effects. Therefore, we employed confocal laser scanning microscopy to observe the colocalization of MPR@PBNPs with lysosomes in endothelial cells at different time points. As shown in Fig. S6A, at the 2-hour incubation time point, MPR@PBNPs exhibited a high degree of colocalization with lysosomes, indicating that MPR@PBNPs were trapped within lysosomes. However, after 6 hours of incubation, MPR@PBNPs were predominantly observed in the cytoplasm. These results demonstrate that MPR@PBNPs can escape from lysosomes and accumulate in the cytoplasm over time, thus enabling their therapeutic efficacy. During the progression of AS, endothelial cells generate excessive ROS under various adverse conditions, leading to oxidative stress and thereby promoting AS development. Inhibiting ROS production in endothelial cells is beneficial for suppressing AS formation. Initially, we assessed the ability of NPs to suppress ROS generation in endothelial cells. HUVECs were treated with LPS to elevate intracellular ROS levels. Fluorescence microscopy and FACS analysis revealed that free PR-PB, PR@PBNPs, and MPR@PBNPs significantly reduced ROS production in LPS-treated HUVECs (Fig. 4A-C). Furthermore, we investigated the effects of NPs on apoptosis induced by TBHP in HUVECs. Treatment with PR@PBNPs and MPR@PBNPs markedly decreased the apoptosis rate of HUVECs (Fig. 4D-F). Studies have demonstrated that endothelial cells at AS plaque sites uptake lipids and transport them into the intima, contributing to AS progression [34- 36]. Consequently, we evaluated the capacity of NPs to inhibit lipid uptake by endothelial cells. Both PR@PBNPs and MPR@PBNPs effectively suppressed lipid uptake in HUVECs (Fig. 4G-H). Collectively, these findings indicate that MPR@PBNPs can efficiently mitigate endothelial oxidative stress, reduce apoptosis in endothelial cells, and inhibit lipid uptake by endothelial cells.

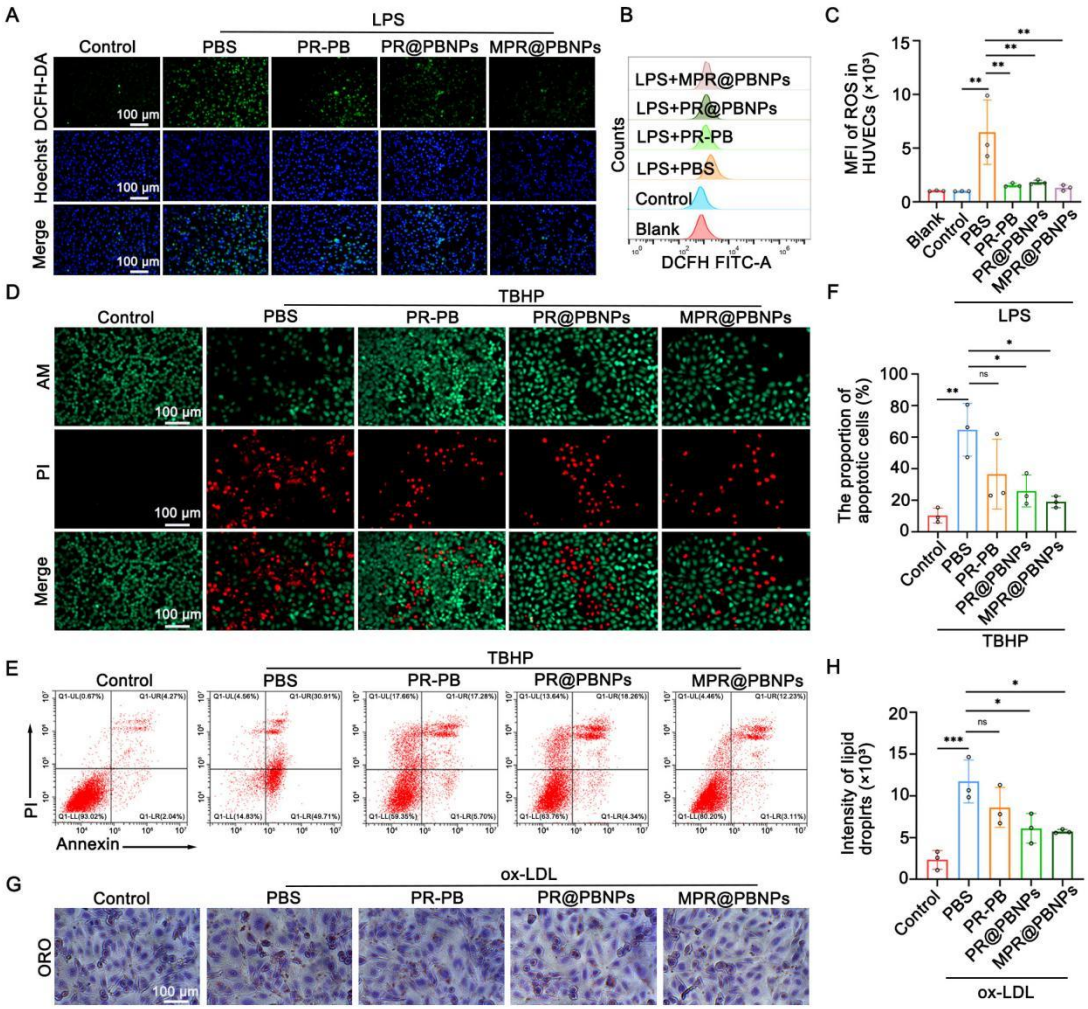



**Figure 4.** MPR@PBNPs inhibit oxidative stress, apoptosis, and ox-LDL uptake of HUVECs (A) Fluorescence images of ROS generated by HUVECs after different treatments (scale bar: 100 μm). (B) FACS analysis profiles and (C) fluorescence quantitative of ROS production levels in HUVECs after different treatments ($n$=3, mean ± SD). (D) Fluorescence images of live/dead cell staining of HUVECs after different treatments (scale bar: 100 μm). (E) Flow cytometry analysis of HUVECs apoptosis after different treatments.. (F) Proportion of HUVECs apoptosis after different treatments ($n$=3, mean ± SD). (G) ORO staining images of HUVECs taken ox-LDL after different treatments. (scale bar:100 μm) (H) Quantitative analysis of intracellular lipid deposition after different treatments. ($n$ = 3, mean ± SD) .*$p$ < 0.05, **$p$ < 0.01, ***$p$ < 0.001.*ns*, no significance.

### 3.5. MPR@PBNPs suppress macrophage ROS production, apoptosis, and foam cell formation

Macrophages are critical cellular participants in AS pathogenesis. The effects of NPs on macrophages were evaluated in vitro. First, the uptake of NPs by RAW264.7 cells was investigated. Compared with PR@PBNPs, more MPR@PBNPs were taken up by inflamed RAW264.7 cells activated by LPS (Fig. 5A-C). Additionally, MPR@PBNPs entered the cytoplasm of RAW264.7 cells following prolonged incubation time (Fig. S6B). These results demonstrate that MPR@PBNPs are effectively internalized by inflamed RAW264.7 cells and can distribute in the cytoplasm, facilitating their therapeutic effects on macrophages. To evaluate the function of NPs in inhibiting macrophages from producing ROS, RAW264.7 cells were stimulated with LPS to induce ROS production. ROS levels were significantly elevated in the PBS-treated group compared to the control group (Fig. 5D). After treatment with free PR-PB, PR@PBNPs, and MPR@PBNPs, the intracellular ROS level was significantly reduced (Fig. 5E-F). Furthermore, MPR@PBNPs effectively suppressed RAW264.7 cells' apoptosis induced by TBHP (Fig. 5G-I). Excessive lipid uptake by macrophages leads to foam cell formation, exacerbating inflammation and plaque progression. ORO staining was employed to evaluate the inhibitory effects of MPR@PBNPs on foam cell formation *in vitro*. Compared with free PR-PB, both PR@PBNPs and MPR@PBNPs significantly suppressed foam cell formation, with MPR@PBNPs demonstrating the strongest inhibitory efficacy (Fig. 5J- K).

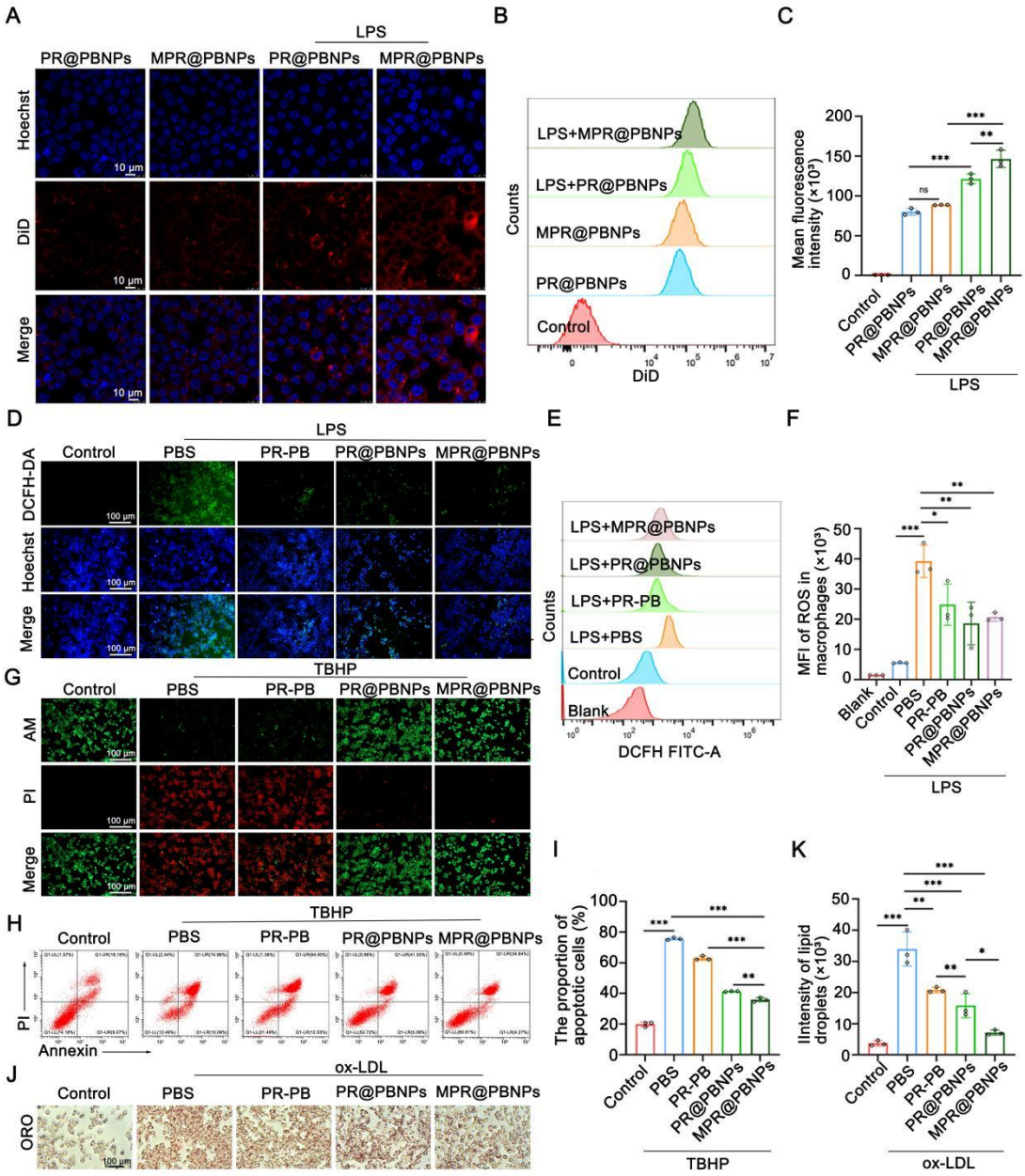



**Figure 5.** In vitro therapeutic effects of MPR@PBNPs on macrophages. (A) Images of PR@PBNPs and MPR@PBNPs taken by normal and LPS-activated RAW264.7 cells. (B) Flow cytometry analysis of PR@PBNPs and MPR@PBNPs taken by normal and LPS-activated RAW264.7 cells. (C) Quantitative fluorescence intensity of PR@PBNPs and MPR@PBNPs uptake in normal and LPS-activated RAW264.7 cells ($n$=3, mean ± SD). (D) Fluorescence images of intracellular ROS levels in RAW264.7 cells after different treatments (scale bar: 100 μm). (E) Flow cytometry analysis of ROS levels in RAW264.7 cells after different treatments. (F) Statistical analysis of ROS fluorescence intensity in RAW264.7 cells after different treatments ($n$=3, mean ± SD). (G) Fluorescence images of live/dead cell staining of RAW264.7 cells after different treatments

(scale bar: 100 μm). (H) Flow cytometry analysis of RAW264.7 cell apoptosis after different treatments. (I) Quantitative analysis of the apoptosis proportion of RAW264.7 cell after different treatments ($n$=3, mean ± SD). (J) ORO staining of ox-LDL-induced foam cell formation in RAW264.7 cells after different treatments (scale bar: 100 μm). (K) Quantitative analysis of intracellular lipid deposition in macrophages ($n$=3, mean ± SD). Statistical significance: *$p$<0.05, **$p$<0.01, ***$p$<0.001.

To further investigate the therapeutic mechanism of MPR@PBNPs in macrophages, we performed whole-transcriptome RNA sequencing and analysis on inflammatory macrophages treated with MPR@PBNPs. As shown in Fig. 6A and 6E, principal component analysis (PCA) and heatmap visualization revealed distinct gene expression profiles among the Control, PBS, and MPR@PBNPs groups. Volcano plots (Fig. 6B-D) demonstrated that compared to the Control group, the PBS group exhibited 3,737 significantly differentially expressed genes (DEGs), comprising 2,666 downregulated and 1,071 upregulated genes. Compared to the PBS group, MPR@PBNPs-treated macrophages showed 1,122 significant DEGs, with 547 downregulated and 575 upregulated genes. Kyoto Encyclopedia of Genes and Genomes (KEGG) and Gene Set Enrichment Analysis (GSEA) (Fig. 6F and H) indicated that MPR@PBNPs treatment significantly downregulated the MAPK signaling pathway, lipid and atherosclerosis pathway, TNF signaling pathway, NF-κB signaling pathway, Toll-like receptor signaling pathway, and IL-17 signaling pathway compared to the PBS group. Furthermore, GO analysis revealed downregulation in molecular functions including NF-κB binding, cell adhesion molecule binding, chemokine receptor binding, and CXCR chemokine receptor binding (Fig. 6G). These results demonstrate that MPR@PBNPs treatment effectively alters the gene expression profile in inflammatory macrophages and modulates pathways associated with oxidative stress, inflammation, and apoptosis.

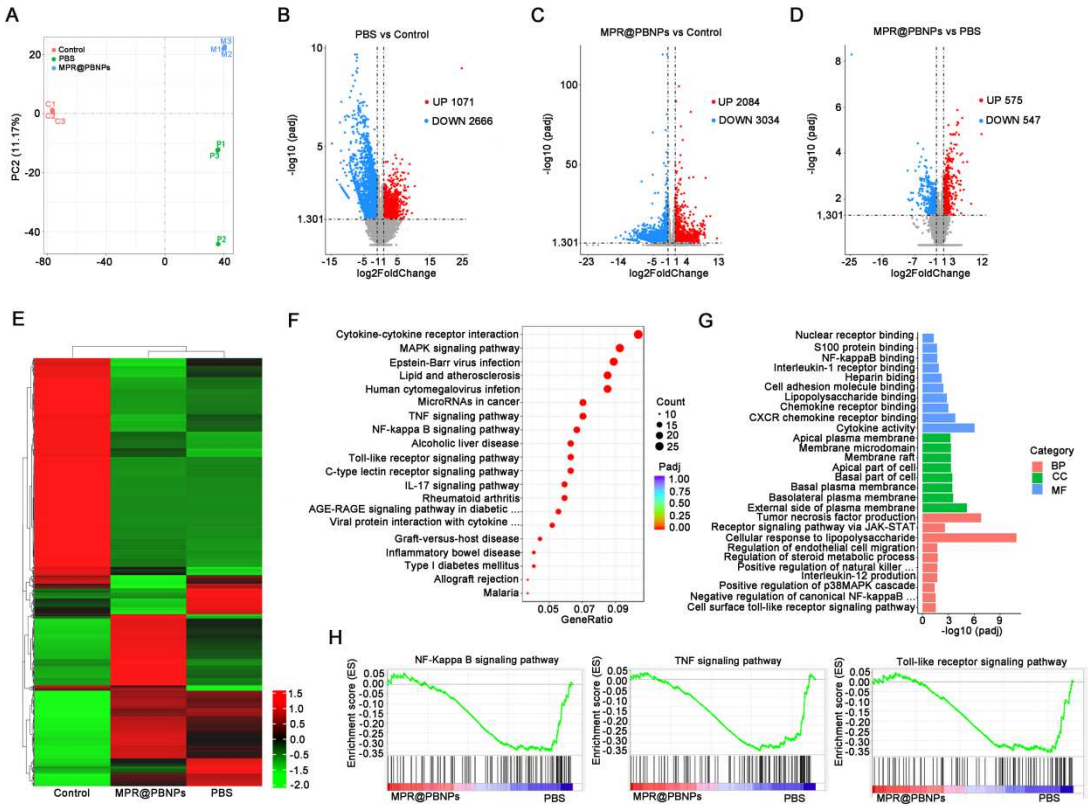



**Figure 6.** RNA transcriptome sequencing of MPR@PBNPs-treated inflammatory macrophages. (A) PCA plot of genes from the Control, PBS, and MPR@PBNPs groups. (B) Volcano plot of DEGs between the PBS and Control groups. (C) Volcano plot of DEGs between the MPR@PBNPs and Control groups. (D) Volcano plot of DEGs between the MPR@PBNPs and PBS groups. （E） Heatmap of clustered DEGs in the Control, MPR@PBNPs, and PBS groups. (F) KEGG pathway enrichment analysis of the top 20 significantly downregulated biological processes in the MPR@PBNPs group compared to the PBS group. (G) GO analysis of biological process (BP), cellular component (CC), and molecular function (MF) terms in the MPR@PBNPs group compared to in PBS group. (H) GSEA of the genes in the NF-κB, TNF and Toll-like receptor signaling pathway in theMPR@PBNPs group compared to in the PBS group.

### 3.6. Targeting effect to atherosclerotic lesions and anti-AS efficacy in vivo of MPR@PBNPs

First, we investigated the *in vivo* targeting capability of MPR@PBNPs to AS lesion areas. AS model mice were intravenously injected with DiD-labeled PR@PBNPs or MPR@PBNPs via the tail vein. The aortas and major organs were harvested for fluorescence imaging 24 h post-injection. Compared to PR@PBNPs, MPR@PBNPs showed more pronounced accumulation at the aortas, demonstrating MPR@PBNPs efficient targeting of AS lesions (Fig. 7A, C and S7). Furthermore, both PR@PBNPs and MPR@PBNPs predominantly accumulated in the liver, indicating their primary hepatic clearance (Fig. 7B and D). To investigate the therapeutic efficacy of MPR@PBNPs against AS in vivo, AS model mice were divided into four groups and treated with 5% glucose, free PR+PB, PR@PBNPs, or MPR@PBNPs, respectively. ORO staining of the aortas revealed that the MPR@PBNPs-treated group exhibited the smallest plaque area compared to other groups (Fig. 7E-F and S8). Further analysis of aortic root plaques demonstrated that MPR@PBNPs significantly reduced intraplaque lipid deposition, necrotic core formation, and collagen deposition compared to control treatments. Additionally, MPR@PBNPs effectively decreased smooth muscle cell and macrophage content within plaques (Fig. 7G-L). These results conclusively demonstrate that MPR@PBNPs potently inhibit AS plaque progression.

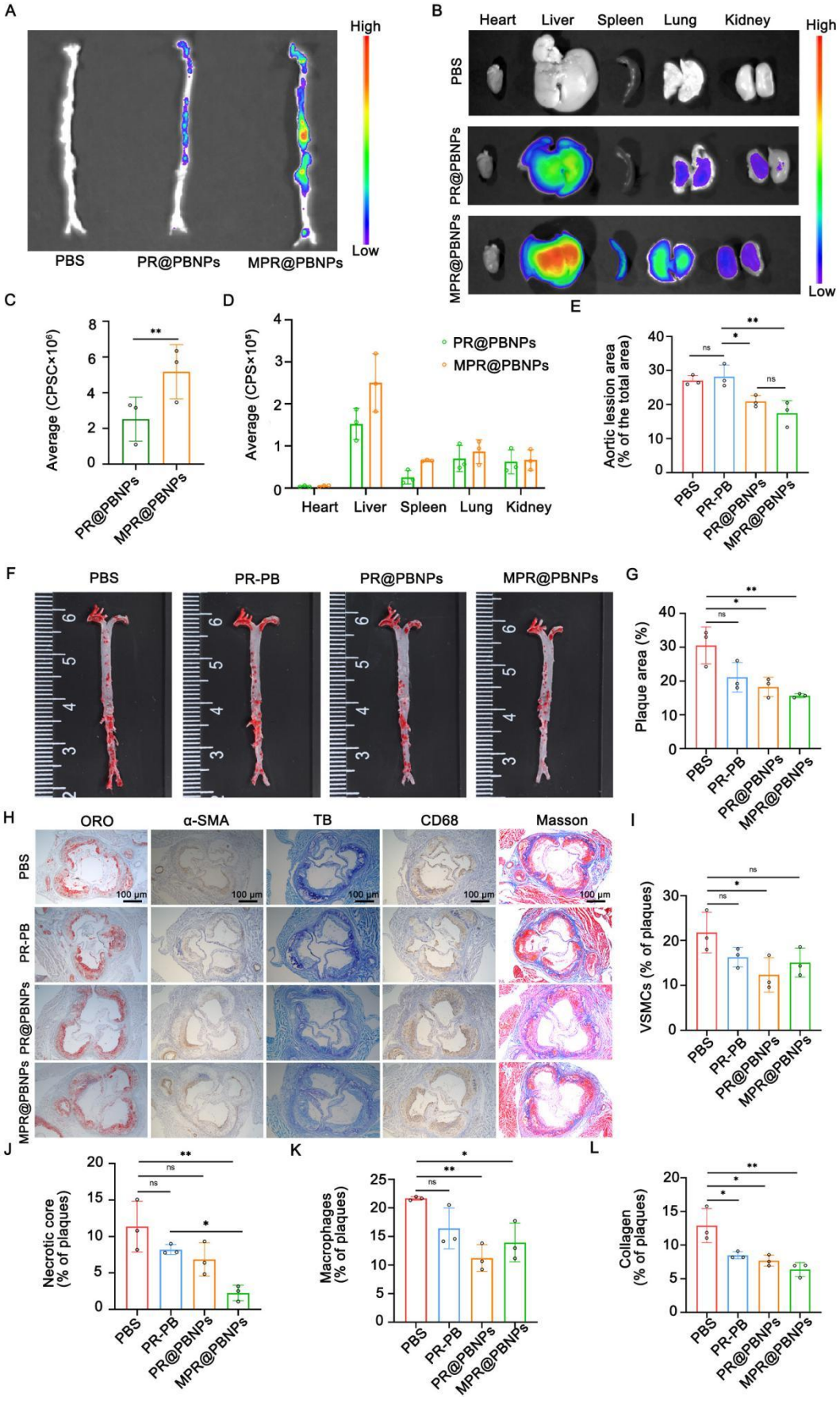

A
High
Low
PBS
PR@PBNPs
MPR@PBNPs
B
Heart
Liver
Spleen
Lung
Kidney
High
Low
PBS
PR@PBNPs
MPR@PBNPs
C
Average (CPSC×10⁶)
PR@PBNPs
MPR@PBNPs
D
Average (CPS×10⁵)
PR@PBNPs
MPR@PBNPs
Heart
Liver
Spleen
Lung
Kidney
E
Aortic lession area (% of the total area)
PBS
PR-PB
PR@PBNPs
MPR@PBNPs
F
PBS
PR-PB
PR@PBNPs
MPR@PBNPs
G
Plaque area (%)
PBS
PR-PB
PR@PBNPs
MPR@PBNPs
H
ORO
α-SMA
TB
CD68
Masson
PBS
PR-PB
PR@PBNPs
MPR@PBNPs
100 μm
I
VSMCs (% of plaques)
PBS
PR-PB
PR@PBNPs
MPR@PBNPs
J
Necrotic core (% of plaques)
PBS
PR-PB
PR@PBNPs
MPR@PBNPs
K
Macrophages (% of plaques)
PBS
PR-PB
PR@PBNPs
MPR@PBNPs
L
Collagen (% of plaques)
PBS
PR-PB
PR@PBNPs
MPR@PBNPs

**Figure 7.** In vivo therapeutic evaluation of MPR@PBNPs. (A) Fluorescence imaging of PR@PBNPs and MPR@PBNPs accumulation in AS mouse aortas. (B) Fluorescence imaging of PR@PBNPs and MPR@PBNPs accumulation in the major organs. (C) Quantitative fluorescence intensity analysis of PR@PBNPs and MPR@PBNPs accumulation in AS mouse aortas ($n$=3, mean ± SD). (D) Quantitative fluorescence intensity analysis of PR@PBNPs and MPR@PBNPs accumulation in the major organs ($n$=3, mean ± SD). (E) AS lesion area quantification in the aortas of different groups ($n$=3, mean ± SD). (F) Respective images of ORO-stained aortas of different groups. (G) Quantitative analysis of lipid deposition areas in aortic root plaques ($n$=3, mean ± SD). (H) The representative images of aortic root staining: ORO (for lipid staining), α-SMA (for smooth muscle cells), toluidine blue (for necrotic core staining), CD68 (for macrophages staining), Masson's trichrome (for collagen staining) (scale bar: 100 μm). Quantitative percentage ratio of smooth muscle cell positive areas (I), necrotic core areas (J), macrophage positive areas (K). Collagen areas (L), and MMP-9 expression positive areas in aortic root sections of different groups ($n$=3, mean ± SD). Statistical significance: *$p$≤0.05, **$p$≤0.01, ***$p$≤0.001; *ns*, no significance.

### 3.7. In vivo biosafety profile of MPR@PBNPs

Biosafety is paramount for nanotherapeutics. Body weight changes serve as a primary indicator of murine health status, where significant fluctuations may reflect drug toxicity or adverse effects. Throughout the 45-day treatment period, all groups exhibited stable body weight (Fig. S9), providing preliminary confirmation of negligible systemic toxicity. Histopathological evaluation via hematoxylin and eosin (H&E) staining of major organs revealed no observable histopathological abnormalities in the free PR-PB, PR@PBNPs, or MPR@PBNPs treatment groups compared to PBS controls (Fig. 8A). Complete blood count (CBC) analysis showed no statistically significant variations in white blood cells (WBC), red blood cells (RBC), hemoglobin (HGB), or platelets (PLT) across all groups (Fig. 8B). Serum lipid analysis revealed no significant differences in high-density lipoprotein (HDL), low-density lipoprotein (LDL), triglycerides (TG), or total cholesterol (CHO) levels among the treatment groups (Fig. 8C). Furthermore, the primary biochemical parameters remained within

normal physiological ranges across all groups post-treatment, indicating the absence of hepatic or renal functional impairment (Fig. 8D). Collectively, these findings demonstrate that MPR@PBNPs exhibit no apparent toxic side effects and possess a favorable biosafety profile.

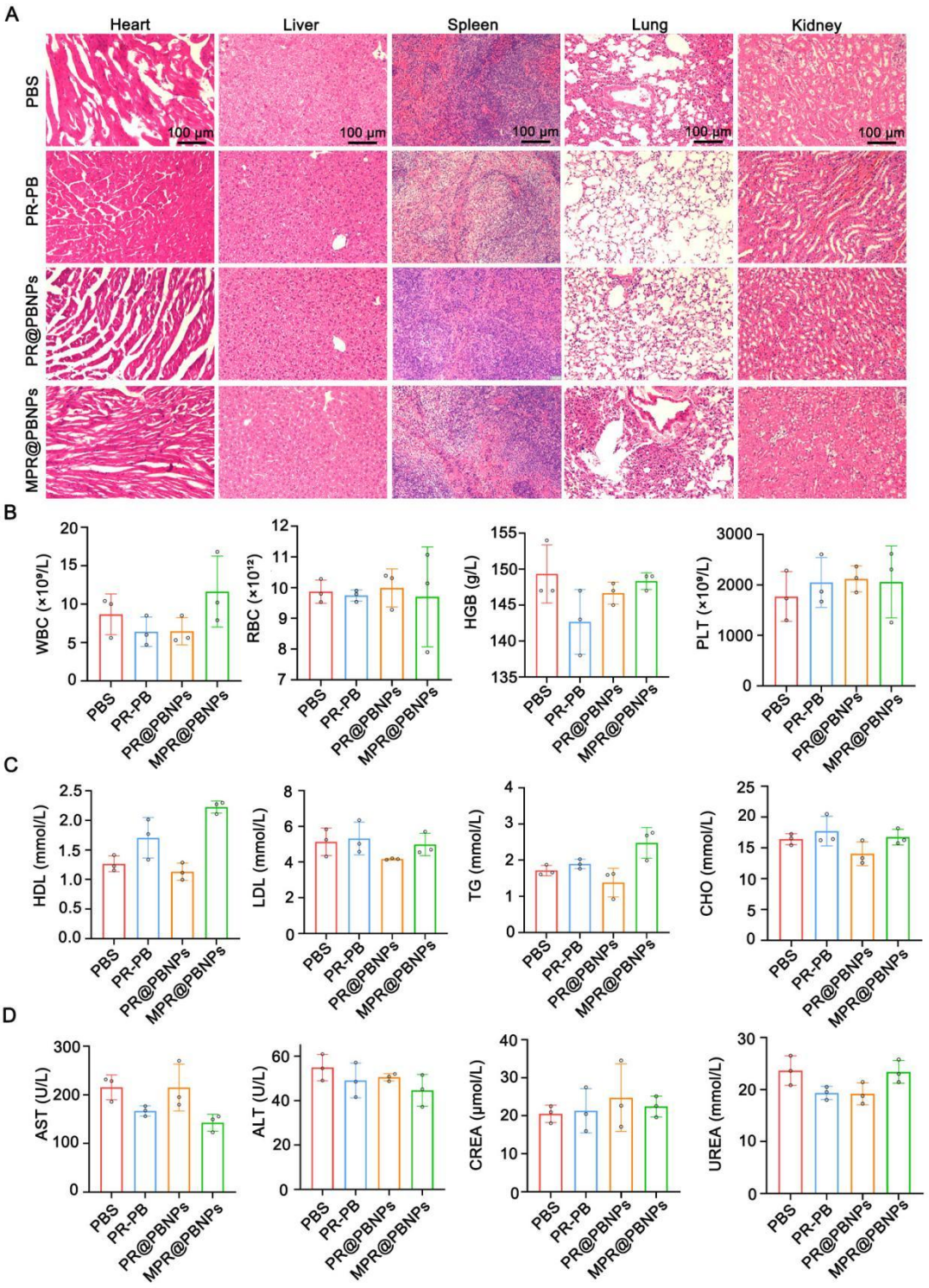


**Figure 8.** Biosafety assessment of MPR@PBNPs in AS model mice. (A) H&E-stained sections of major organs of different groups (scale bar: 100 μm). (B) Main blood routine indicators of mice from different groups: PLT, WBC, RBC, and HGB. (C) Lipid profiles in mouse serum of different groups: HDL, LDL, TG, and CHO. (D) The primary biochemical parameters in mice serum of different groups: AST (aspartate aminotransferase), ALT (alanine aminotransferase), CREA (creatinine), and UREA (blood urea nitrogen). All data represent mean ± SD ($n$=3).

## 4. Conclusion

In this work, inspired by the self-assembly strategy of TCM components, we discovered that PR and PB can co-assemble into stable NPs (PR@PBNPs), achieving efficient co-loading of both PR and PB. To enable effective targeting of AS lesions, we further engineered PR@PBNPs with MM. The resulting MPR@PBNPs exhibited uniform nanoscale size, favorable stability, and retained the protein composition of MM. In vitro experiments demonstrated that MPR@PBNPs possessed good cytocompatibility and effectively inhibited oxidative stress, apoptosis, and lipid uptake in both endothelial cells and macrophages. In AS mouse models, compared to PR@PBNPs, MPR@PBNPs showed significantly enhanced accumulation at AS lesion sites. Furthermore, MPR@PBNPs effectively suppressed AS progression while maintaining excellent biosafety. In conclusion, this study developed a novel biomimetic co-assembled nanoformulation, offering a promising new strategy for targeted AS therapy.

## AUTHOR INFORMATION


### Corresponding Authors

**Li Fu** − The Eighth Affiliated Hospital of Sun Yat-sen University, Shenzhen 518033, China; Geriatrics Department, Neurological Rehabilitation Department, The Eighth Affiliated Hospital of Sun Yat-sen University, Shenzhen 518033, China; Email: fuliruo302@163.com

**Guixue Wang** − JinFeng Laboratory, Chongqing, 401329, China; Key Laboratory for Biorheological Science and Technology of the Ministry of Education, National Local Joint Engineering Lab for Vascular Implants, College of Bioengineering, Chongqing University, Chongqing, 400044, China; Email: wanggx@cqu.edu.cn

**Yi Wang** − School of Basic Medical Sciences, Chongqing Medical University, Chongqing, 400016, China; JinFeng Laboratory, Chongqing, 401329, China; Email: wangyi@cqmu.edu.cn

---

**Authors**

**Yan Gao** − School of Basic Medical Sciences, Chongqing Medical University, Chongqing, 400016, China

**Yangyang Bai** − School of Basic Medical Sciences, Chongqing Medical University, Chongqing, 400016, China

**Jieying Zeng** − School of Basic Medical Sciences, Chongqing Medical University, Chongqing, 400016, China

**Yinuo Wang** − Chongqing Medical University-University of Leicester Joint Institute, Chongqing Medical University, Chongqing, 400016, China

**Yuxin Zhang** − School of Basic Medical Sciences, Chongqing Medical University, Chongqing, 400016, China

**Mengjie Jia** − Department of Critical Care Medicine, The First Affiliated Hospital of Chongqing Medical University, Chongqing 400010, China

**Yajie Guo** − School of Basic Medical Sciences, Chongqing Medical University, Chongqing, 400016, China

**Juhui Qiu** − Key Laboratory for Biorheological Science and Technology of the Ministry of Education, National Local Joint Engineering Lab for Vascular Implants, College of Bioengineering, Chongqing University, Chongqing, 400044, China

**Yiliang Li** − The Eighth Affiliated Hospital of Sun Yat-sen University, Shenzhen 518033, China

## Acknowledgements

The author thanks the support from the Public Experiment Center of State Bioindustrial Base (Chongqing) China.

## Ethics statement

This study and included experimental procedures were approved by the institutional animal care and use committee of Chongqing Medical University (Approval No. IACUC-CQMU-2023-0385). All animal housing and experiments were conducted in strict accordance with the institutional guidelines for the care and use of laboratory animals.

## Appendix A. Supplementary data

The following is the Supplementary data to this article:

## Funding

This work was supported by the National Natural Science Foundation of China (32201150, 32471366, 12032007, 82271321), the Science and Technology Innovation Project of Jinfeng Laboratory, Chongqing, China (jfkyjf202203001), the Natural Science Foundation of Chongqing (CSTB2022NSCQ-MSX0096), Futian Healthcare Research Project（NO. FTWS034）Shenzhen Science and Technology Program (JCYJ20220530144415035, JCYJ20230807111011024), and Chongqing Traditional Chinese Medicine Innovation Team Construction Project (2023110002).

## Conflict of Interest Statement

The authors declare no competing financial interest.

## Data Availability Statement

The data that support the findings of this study are available from the corresponding author upon reasonable request.

## Consent for publication

All authors of this study agreed to publish.

## Authors' contributions

Yan Gao: Writing – original draft, Validation, Software, Investigation, Data curation, Conceptualization.Yangyang Bai: Software, Methodology, Data curation. Jieying Zeng: Writing – review & editing, Validation, Software, Methodology, Investigation, Data curation. Yinuo Wang: Validation, Methodology, Data curation. Yuxin Zhang: Methodology, Data curation. Mengjie Jia: Methodology, Investigation, Data curation. Yajie Guo: Visualization, Software, Methodology. Juhui Qiu: Writing – review & editing, Supervision. Yiliang Li: Writing – review & editing, Supervision. Li Fu: Validation, Supervision, Conceptualization. Guixue Wang: Writing – review & editing, Validation, Supervision, Project administration, Funding acquisition, Conceptualization. Yi Wang: Writing – review & editing, Validation, Supervision, Project administration, Funding acquisition, Conceptualization.

## References


1. Kobiyama, K.; Ley, K. Atherosclerosis. *Circ. Res.* 2018, *123* (10), 1118–1120.
2. Libby, P. The changing landscape of atherosclerosis. *Nature* 2021, *592* (7855), 524–533.
3. Bäck, M.; Yurdagul, A.; Tabas, I.; Öörni, K.; Kovanen, P. T. Inflammation and its resolution in atherosclerosis: mediators and therapeutic opportunities. *Nat. Rev. Cardiol.* 2019, *16* (7), 389–406.
4. Hetherington, I.; Totary-Jain, H. Anti-atherosclerotic therapies: Milestones, challenges, and emerging innovations. *Mol. Ther.* 2022, *30* (10), 3106–3117.
5. Ma, B.; Xiao, Y.; Lv, Q.; Li, G.; Wang, Y.; Fu, G. Targeting Theranostics of Atherosclerosis by Dual-Responsive Nanoplatform via Photoacoustic Imaging and Three-In-One Integrated Lipid Management. *Adv. Mater.* 2023, *35* (5), 2206129.
6. Falk, E. Pathogenesis of Atherosclerosis. *J. Am. Coll. Cardiol.* 2006, *47* (8, Suppl.), C7–C12.
7. Zhang, S.; Liu, Y.; Cao, Y.; Zhang, S.; Sun, J.; Wang, Y.; Song, S.; Zhang, H. Targeting the Microenvironment of Vulnerable Atherosclerotic Plaques: An Emerging Diagnosis and Therapy Strategy for Atherosclerosis. *Adv. Mater.* 2022, *34* (29), 2110660.
8. Tao, Y.; Lan, X.; Zhang, Y.; Fu, C.; Liu, L.; Cao, F.; Guo, W. Biomimetic nanomedicines for precise atherosclerosis theranostics. *Acta Pharm. Sin. B* 2023, *13* (11), 4442–4460.

9. Aili, T.; Zong, J.-B.; Zhou, Y.-F.; Liu, Y.-X.; Yang, X.-L.; Hu, B.; Wu, J.-H. Recent advances of self-assembled nanoparticles in the diagnosis and treatment of atherosclerosis. *Theranostics* 2024, *14* (19), 7505–7533.

10. He, Z.; Chen, W.; Hu, K.; Luo, Y.; Zeng, W.; He, X.; Li, T.; Ouyang, J.; Li, Y.; Xie, L.; et al. Resolvin D1 delivery to lesional macrophages using antioxidative black phosphorus nanosheets for atherosclerosis treatment. *Nat. Nanotechnol.* 2024, *19* (9), 1386–1398.

11. Aili, T.; Zong, J. B.; Zhou, Y. F.; Liu, Y. X.; Yang, X. L.; Hu, B.; Wu, J. H. Recent advances of self-assembled nanoparticles in the diagnosis and treatment of atherosclerosis. *Theranostics* 2024, *14* (19), 7505–7533.

12. Jun, H.; Jeon, C.; Kim, S.; Song, N. Nanoassemblies of Self-Immolative Boronate-Bridged Retinoic Acid Dimeric Prodrug as a Clot-Targeted Self-Deliverable Antithrombotic Nanomedicine. *ACS Nano* 2023, *17* (13), 12336–12346.

13. Su, M.; Dai, Q.; Chen, C.; Zeng, Y.; Chu, C.; Liu, G. Nano-Medicine for Thrombosis: A Precise Diagnosis and Treatment Strategy. *Nano-Micro Lett.* 2020, *12* (1), 96.

14. (14) Guan, Q.; Dou, H. Thrombus-Targeting Polymeric Nanocarriers and Their Biomedical Applications in Thrombolytic Therapy. *Front. Physiol.* 2021, *12*, 763085.

15. Huang, J.; Zhu, Y.; Xiao, H.; Liu, J.; Li, S.; Zheng, Q.; Tang, J.; Meng, X. Formation of a traditional Chinese medicine self-assembly nanostrategy and its application in cancer: a promising treatment. *Chin. Med.* 2023, *18* (1), 66.

16. Tian, X.; Wang, P.; Li, T.; Huang, X.; Guo, W.; Yang, Y.; Yan, M.; Zhang, H.; Cai, D.; Jia, X.; et al. Self-assembled natural phytochemicals for synergistically antibacterial application from the enlightenment of traditional Chinese medicine combination. *Acta Pharm. Sin. B* 2020, *10* (9), 1784–1795.

17. Mao, Q.; Min, J.; Zeng, R.; Liu, H.; Li, H.; Zhang, C.; Zheng, A.; Lin, J.; Liu, X.; Wu, M. Self-assembled traditional Chinese nanomedicine modulating tumor immunosuppressive microenvironment for colorectal cancer immunotherapy. *Theranostics* 2022, *12* (14), 6088–6105.

18. He, H.; Han, Q.; Wang, S.; Long, M.; Zhang, M.; Li, Y.; Zhang, Y.; Gu, N. Design of a Multifunctional Nanozyme for Resolving the Proinflammatory Plaque Microenvironment and Attenuating Atherosclerosis. *ACS Nano* 2023, *17* (15), 14555–14571.

19. Kong, P.; Cui, Z.-Y.; Huang, X.-F.; Zhang, D.-D.; Guo, R.-J.; Han, M. Inflammation and atherosclerosis: signaling pathways and therapeutic intervention. *Signal Transduct. Targeted Ther.* 2022, *7* (1), 131.

20. Kasikara, C.; Doran, A. C.; Cai, B.; Tabas, I. The role of non-resolving inflammation in atherosclerosis. *J. Clin. Invest.* 2018, *128* (7), 2713–2723.

21. Zhou, Y. X.; Zhang, H.; Peng, C. Puerarin: a review of pharmacological effects. *Phytother. Res.* 2014, *28* (7), 961–975.

22. Yang, M.; Xia, L.; Song, J.; Hu, H.; Zang, N.; Yang, J.; Zou, Y.; Wang, L.; Zheng, X.; He, Q.; et al. Puerarin ameliorates metabolic dysfunction-associated fatty liver disease by inhibiting ferroptosis and inflammation. *Lipids Health Dis.* 2023, *22* (1), 202.

23. Chen, T.; Liu, W.; Xiong, S.; Li, D.; Fang, S.; Wu, Z.; Wang, Q.; Chen, X. Nanoparticles Mediating the Sustained Puerarin Release Facilitate Improved Brain Delivery to Treat Parkinson's Disease. ACS Appl. Mater. Interfaces 2019, 11 (48), 45276–45289.

24. Sharif, A.; Mamo, J.; Lam, V.; Al-Salami, H.; Mooranian, A.; Watts, G. F.; Clarnette, R.; Luna, G.; Takechi, R. The therapeutic potential of probucol and probucol analogues in neurodegenerative diseases. *Transl. Neurodegener.* 2024, *13* (1), 6.

25. Fu, X.; Yu, X.; Jiang, J.; Yang, J.; Chen, L.; Yang, Z.; Yu, C. Small molecule-assisted assembly of multifunctional ceria nanozymes for synergistic treatment of atherosclerosis. *Nat. Commun.* 2022, *13* (1), 6528.

26. Jia, M.; Miao, W.; Li, Y.; Guo, Y.; Zeng, J.; Gao, Y.; Li, X.; Wang, Y.; Zhao, Z.; Xu, Z.; et al. A polymerized probucol nanoformulation with neutrophil extracellular vesicle camouflage for cerebral ischemia-reperfusion injury therapy. *Innovation* 2025, *6* (4), 100761.

27. Fang, R. H.; Gao, W.; Zhang, L. Targeting drugs to tumours using cell membrane-coated nanoparticles. *Nat. Rev. Clin. Oncol.* 2023, *20* (1), 33–48.

28. Fang, R. H.; Kroll, A. V.; Gao, W.; Zhang, L. Cell Membrane Coating Nanotechnology. *Adv. Mater.* 2018, *30* (23), e1706759.

29. Luk, B. T.; Zhang, L. Cell membrane-camouflaged nanoparticles for drug delivery. *J. Control. Release* 2015, *220* (Pt B), 600–607.

30. Zhao, Y.; Li, Q.; Niu, J.; Guo, E.; Zhao, C.; Zhang, J.; Liu, X.; Wang, L.; Rao, L.; Chen, X.; et al. Neutrophil Membrane-Camouflaged Polyprodrug Nanomedicine for Inflammation Suppression in Ischemic Stroke Therapy. *Adv. Mater.* 2024, *36* (21), e2311803.

31. Zeng, J.; Zhang, Y.; Gao, Y.; Jia, M.; Guo, Y.; Li, X.; Wang, Y.; Zhao, C.; Qiu, J.; McGinty, S.; et al. Biomimetic Ginsenoside Rb1 and Probucol Co-Assembled Nanoparticles for Targeted Atherosclerosis Therapy via Inhibition of Oxidative Stress, Inflammation, and Lipid Deposition. *ACS Nano* 2025, *19* (25), 22968–22987.

32. Wang, Y.; Zhang, K.; Qin, X.; Li, T.; Qiu, J.; Yin, T.; Huang, J.; McGinty, S.; Pontrelli, G.; Ren, J.; et al. Biomimetic Nanotherapies: Red Blood Cell Based

Core–Shell Structured Nanocomplexes for Atherosclerosis Management. *Adv. Sci.* 2019, *6* (12), 1900172.

33. Zhang, Y.; Zhang, H.; Zhao, F.; Jiang, Z.; Cui, Y.; Ou, M.; Mei, L.; Wang, Q. Mitochondrial-targeted and ROS-responsive nanocarrier via nose-to-brain pathway for ischemic stroke treatment. *Acta Pharm. Sin. B* 2023, *13* (12), 5107–5120.

34. Pirri, D.; Tian, S.; Tardajos-Ayllon, B.; Irving, S. E.; Donati, F.; Allen, S. P.; Mammoto, T.; Vilahur, G.; Kabir, L.; Bennett, J.; et al. EPAS1 Attenuates Atherosclerosis Initiation at Disturbed Flow Sites Through Endothelial Fatty Acid Uptake. *Circ. Res.* 2024, *135* (8), 822–837.

35. Huang, L.; Chambliss, K. L.; Gao, X.; Yuhanna, I. S.; Behling-Kelly, E.; Bergaya, S.; Ahmed, M.; Michaely, P.; Luby-Phelps, K.; Darehshouri, A.; et al. SR-B1 drives endothelial cell LDL transcytosis via DOCK4 to promote atherosclerosis. *Nature* 2019, *569* (7757), 565–569.

36. Sawamura, T.; Kume, N.; Aoyama, T.; Moriwaki, H.; Hoshikawa, H.; Aiba, Y.; Tanaka, T.; Miwa, S.; Katsura, Y.; Kita, T.; et al. An endothelial receptor for oxidized low-density lipoprotein. *Nature* 1997, *386* (6620), 73–77.

## Supplementary Files

This is a list of supplementary files associated with this preprint. Click to download.

- SupportingInformation.docx